Tectonophysics 479 (2009) 4–18

Contents lists available at ScienceDirect

Tectonophysics

journal homepage: www.elsevier.com/locate/tecto

Interseismic crustal deformation in the Taiwan plate boundary zone revealed by GPS observations, seismicity, and earthquake focal mechanisms

Ya-Ju Hsu [a,*], Shui-Beih Yu [a], Mark Simons [b], Long-Chen Kuo [a], Horng-Yue Chen [a]

[a] Institute of Earth Sciences, Academia Sinica, P.O. Box 1-55, Nankang, Taipei, Taiwan
[b] Division of Geological and Planetary Sciences, California Institute of Technology, Pasadena, CA 91125, USA

ARTICLE INFO

Article history:
Received 29 May 2008
Received in revised form 11 November 2008
Accepted 18 November 2008
Available online 3 December 2008

Keywords:
Taiwan
Strain rate
Seismicity
Earthquake focal mechanism
GPS

ABSTRACT

We use GPS-derived surface velocities, seismicity, as well as estimates of earthquake focal mechanisms from the time period before the 1999 Chi-Chi earthquake to evaluate spatial variations of surface strain rate and crustal stress regime in the Taiwan plate boundary zone. We estimate strain rates with a new but simple approach that solves for surface velocity on a rectangular grid while accounting for the distance between observations and each grid node and the impact of a spatially variable density of observations. This approach provides stable and interpretable strain-rate estimates. In addition, we perform a stress tensor inversion using earthquake focal mechanisms determined by P waves first-motion polarities. Our estimates of the principal orientations of two-dimensional surface strain rate tensor generally agree with the inferred orientations of the stress axes. This agreement suggests that a large scale variation of stress orientations from the surface to the base of the crust is insignificant and the predicted faulting style is consistent with stress buildup during the interseismic loading. We find that the geometric configuration of the Chinese continental margin alone cannot fully explain the distribution of maximum contraction and compressive axes in Taiwan. Distribution of seismicity and focal mechanisms before and after the Chi-Chi mainshock suggest that the maximum principal stress axis is vertically-oriented in the Central Range; in contrast to the horizontal maximum principal stress axis in western Taiwan and the Longitudinal Valley. Extension in the Central Range reflects the consequence of exhumation and crustal thickening.

1. Introduction

The island of Taiwan is located in the plate boundary zone between the Eurasian (EUP) and Philippine Sea plates (PHP) and is bound by two subduction zones. In the north, the PHP subducts beneath the Ryukyu Arc; while to the south, the South China Sea block of the EUP subducts beneath the PHP (Fig. 1). The Taiwan orogeny results from the collision of the Luzon volcanic arc in the PHP and the Chinese continental margin in the EUP beginning about 3–6 Ma ago (Suppe, 1984; Barrier and Angelier, 1986; Teng, 1996; Huang et al., 1997). The plate convergence rate across the Island is about 80 mm/yr in a direction of N310°E (Seno et al., 1993; Yu et al., 1997).

Taiwan can be divided into six northeast-trending physiographic regions which are separated by major faults (Fig. 1). These regions are, from west to east, the Coastal Plain, the Western Foothills, the Hsueshan Range, the Central Range, the Longitudinal Valley, and the Coastal Range. The Coastal Plain is composed of Quaternary alluvial deposits derived from the Western Foothills and the Central Range. The Western Foothills consists of a thick sequence of shallow marine to shelf sediments from the late Oligocene, Miocene, to early Pleistocene. The Hsueshan Range is mostly composed of Eocene and Oligocene sediments. The Central Range is characterized by Tertiary metamorphism, in contrast with the adjacent non-metamorphic rocks in the Western Foothills. The 150 km long NNE-trending Longitudinal Valley separates the Central Range to the west and the Coastal Range to the east. Quaternary clastic fluvial sediments fill this valley. The Coastal Range is composed of Neogene andesitic volcanic rocks of the northern Luzon Arc. The Longitudinal Valley Fault (LVF) runs more or less along the western margin of the Coastal Range and it is a major active structure in eastern Taiwan (Biq, 1972; Hsu, 1976; Wu, 1978; Barrier and Angelier, 1986; Ho, 1986).

An island-wide GPS network composed of more than 195 campaign-mode sites and 17 continuous stations has been established by the Institute of Earth Sciences, Academia Sinica, Ministry of the Interior (MOI) and other institutions since 1989. Most of the campaign-mode sites have been occupied at least once annually since 1990. The first velocity field in the Taiwan area was estimated from the 1990–1995 GPS observations by Yu et al. (1997). The convergence across the Taiwan arc-continent collision zone inferred from GPS velocity field is about 80 mm/yr in the northwest direction. The crustal strain is accumulated in two major zones: the fold-and-thrust belt in the Western Foothills, and the Longitudinal Valley as well as the Coastal Range in eastern Taiwan.

---

* Corresponding author. Tel.: +886 2 27839910x415; fax: +886 2 27839871.
E-mail address: yaru@earth.sinica.edu.tw (Y.J. Hsu).

0040-1951/$ – see front matter © 2008 Elsevier B.V. All rights reserved.
doi:10.1016/j.tecto.2008.11.016

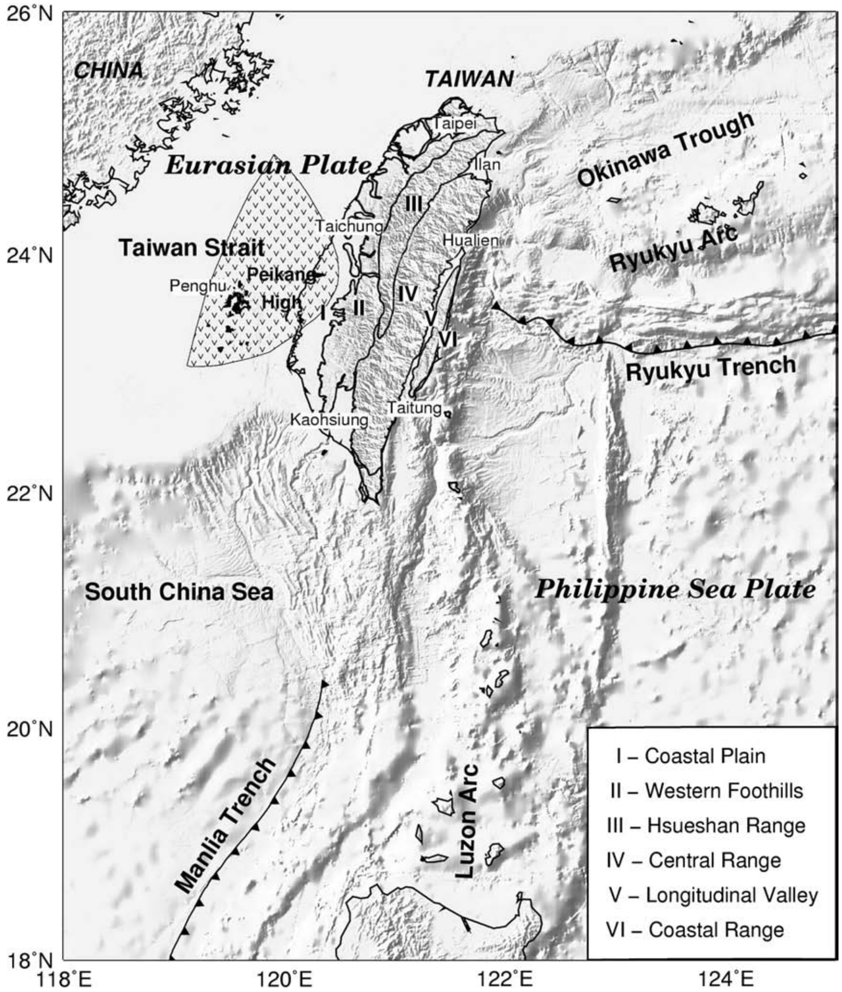

Fig. 1. Tectonic setting in the Taiwan plate boundary zone. In the north, the Philippine Sea plate subducts beneath the Ryukyu Arc; while to the south, the South China Sea block of the Eurasian plate subducts beneath the Philippine Sea plate. The grey colors show the shaded relief topography and bathymetry. Hatched area indicates the Peikang basement high in the Chinese continental margin.

On 21 September 1999, the M_w 7.6 devastating Chi-Chi earthquake struck central Taiwan. The Chi-Chi earthquake resulted from the reactivation of the Chelungpu Fault (CLPF), a major frontal thrust within the Western Foothills (Fig. 2). Most of the GPS sites were affected by this large event and showed significant coseismic movements.

For studying the interseismic deformation before the 1999 Chi-Chi earthquake, we derive an updated Taiwan velocity field using all available campaign-mode and continuous GPS data collected between 1993 and 1999. We use this velocity field sampled at irregular points to estimate velocities sampled on an arbitrarily fine regular rectangular grid. To obtain a continuous strain-rate field, we compute strain rates from gradients of interpolated velocities. The details of methods are presented in a later section after describing the input GPS-derived velocity observations. We then compare principal strain-rate axes with stress axes derived from earthquake focal mechanisms and discuss their implications. In addition, we provide new insights into the crustal stress field in the Taiwan region.

Previous studies based on fault slip data (Angelier et al., 1986), earthquake focal mechanisms (Yeh et al., 1991), borehole breakout data (Suppe et al., 1985) as well as GPS data (Bos et al., 2003; Chang et al., 2003) demonstrate a fan-shaped pattern of maximum compressive or contraction axes in Taiwan. This feature is believed to be affected by the shape of the Chinese continental margin (Hu et al., 1996). However, our study shows the correlation between the trends of the maximum contraction or compressive axes and the shape of the Chinese continental margin is not perfect. Furthermore, we find that the lateral extrusion in SW Taiwan may not fully explain the sharp variations of strain-rate and stress axes between SW Taiwan and the southern Central Range. The tectonic escape in SW Taiwan is previously inferred from sandbox experiments (Lu and Malavieille, 1994). Data sets based on geological, geodetic and seismological evidences also support this hypothesis (Lu and Malavieille, 1994; Lacombe et al., 2001; Bos et al., 2003; Gourley, 2006; Gourley et al., 2007; Hu et al., 2007). The mechanism of the lateral extrusion is perhaps due to low lateral confining stress offshore SW Taiwan and the presence of the Peikang basement high as a rigid indenter (Hu et al., 1996). However, direct onland structural evidence of tectonic extrusion is poor. Based on Quaternary paleostress patterns that that the lateral extrusion have began recently, during the late Pleistocene (Lacombe et al., 2001). On the other hand, we discuss the extension in the Central Range that was first inferred by GPS observations (Yu and Chen, 1994) and was later confirmed by structural fabrics (Crespi et al., 1996) and inferences of the GPS strain-rate field (Bos et al., 2003; Chang et al., 2003). Previous studies suggest that the extension in the Central Range resulted from crustal exhumation after the subduction of the South China Sea block (Lin, 2000). The exhumation occurred when the increase of buoyancy forces on the light subducted continental crust is sufficient to produce decoupling at the base of the crust (Lin, 2000). Recent work suggests that the extension in northeastern Central Range may be driven by the current collision

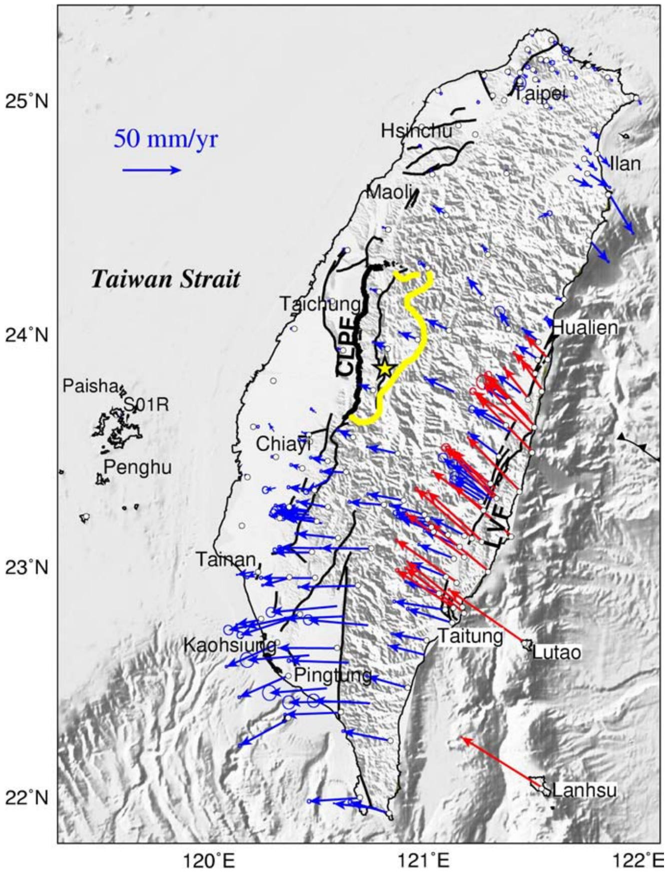

Fig. 2. Taiwan GPS velocity field relative to Paisha, Penghu between 1993 and 1999. Blue and red vectors with 95% confidence ellipses show velocities of sites located to the west and to the east of the Longitudinal fault (LVF), respectively. The grey color shaded relief indicates the topography. Major faults are indicated as black lines. White dots correspond to GPS stations. The star denotes the epicenter of 1999 Chi-Chi earthquake. The area between the CLPF and the yellow line indicates the region where the Chi-Chi coseismic slip is larger than 1 m.

between the PHP and the basement high indenter (Gourley et al., 2007); while the extension in the southern Central Range could be due to the lateral extrusion in SW Taiwan (Gourley, 2006). We suggest that the extension in the Central Range may be a result of exhumation associated with overthickened continental crust or the buoyancy force of the subducted continental crust (Lin, 2000). Detailed discussions can be found in Section 4.

2. Velocity field

We use GPS data from between 1993 and 1999 (before the 1999 Chi-Chi earthquake), including 195 campaign-mode sites and 17 continuous stations operated by the Institute of Earth Sciences, Academia Sinica (IES), Ministry of the Interior (MOI) and other institutions. To minimize the impact of atmospheric disturbance in the GPS observations at sub-tropical areas, we divide the full GPS network into several subnets and conduct surveys at each subnet more or less in the same season every year. The surveys at various subnets can be conducted during different seasons of the year. Most of campaign-mode sites used in this study were occupied at least 5 times during this period. We processed the campaign-mode and continuous GPS data using the Bernese v.4.2 software (Hugentobler et al., 2001) with precise ephemerides from the International GNSS services (IGS). The entire GPS data sets are in a consistent reference frame, the International Terrestrial Reference Frame 1997 (ITRF97), by taking the ITRF97 coordinates and velocities of an IGS core site, TSKB (Tsukuba, Japan) as a reference station. Yu and Kuo (2001) give a more detailed description of the procedures for our GPS data acquisition and processing. The normal equations of single-session solutions for a campaign are first combined to create a campaign solution. An annual survey campaign for a specific area usually spans 10–15 days. The multi-year campaign solutions are then combined to estimate the station velocities (Fig. 2). Comparing to previous results of GPS observations between 1991 and 1995 (Yu et al., 1997), the GPS data used in this study is more robust due to the improvement of technology by increasing amount of GPS satellites and using high precision GPS satellite orbits. In addition, more GPS data coverage in time and space facilitate the detection of subtle signals for crustal deformation.

The Taiwan interseismic velocity field derived from 1993–1999 GPS measurements is shown in Fig. 2 and also given with pertinent data in Table 1. The Paisha, Penghu, continuous GPS station (S01R), situated on the relatively stable Chinese continental margin, is chosen as the reference site. With respect to Penghu, the GPS velocity increases from north to south in the Coastal Plain and the Western Foothills; the maximum rates are mostly less than 5 mm/yr in northern Taiwan, ~25 mm/yr near central Taiwan, then up to ~40 mm/yr in southern Taiwan. The azimuth of GPS velocity also rotates counterclockwise from N70°W near Maoli-Taichung, to N120°W near Kaohsiung. It is worth noting that GPS velocities vary from ~20 mm/yr south of Tainan to ~50 mm/yr near the Kaohsiung area along the coast (Fig. 2) and the deviation in velocity azimuth is small (less than 15°). This feature may imply the existence of a NE–SW trending shear zone between Tainan and Kaohsiung. In eastern Taiwan, the accumulated crustal strain is mainly accommodated in the NNE trending LVF, bounded by the Longitudinal Valley and the Coastal Range. The velocity in the eastern side of the LVF, the Coastal Range, is 26–68 mm/yr in the direction of ~N50°W; whereas that in the western side of the LVF decreases to 18–35 mm/yr in the direction of ~N70°W. The velocity discontinuity across the LVF is about 30 mm/yr. The crustal strain in this region is mainly taken up by aseismic slip, especially near the surface, and earthquakes at greater depths (Yu and Kuo, 2001). In the Ilan plain of northeastern Taiwan, the velocity vectors trend to the southeast with rates of 8–38 mm/yr. This direction is remarkably different from other regions in Taiwan.

3. Method to estimate strain-rate field

In order to obtain a continuous strain-rate field that ensures compatibility, we first estimate a spatially continuous surface velocity field. We adopt a 0.125°×0.125° grid extending from 120°E to 122.25°E and 22°N to 25.25°N. We then estimate the east and north components of horizontal velocities at each node using 212 observed GPS horizontal velocities. The contribution of any given observation is weighted as a function that decays with increasing distance from the estimation point (Shen et al., 1996; Ward, 1998). The estimation equation can be written as:

$$\begin{bmatrix} \mathbf{v}_{\mathrm{e}}^{1} \\ \mathbf{v}_{\mathrm{e}}^{2} \\ \vdots \\ \mathbf{v}_{\mathrm{e}}^{i} \\ \mathbf{v}_{\mathrm{n}}^{1} \\ \mathbf{v}_{\mathrm{n}}^{1} \\ \vdots \\ \mathbf{v}_{\mathrm{n}}^{i} \end{bmatrix} = \begin{bmatrix} \mathbf{O}_{ij} & 0 \\ 0 & \mathbf{O}_{ij} \end{bmatrix} \begin{bmatrix} \widehat{\mathbf{v}}_{\mathrm{e}}^{1} \\ \widehat{\mathbf{v}}_{\mathrm{e}}^{2} \\ \vdots \\ \widehat{\mathbf{v}}_{\mathrm{e}}^{j} \\ \widehat{\mathbf{v}}_{\mathrm{n}}^{1} \\ \widehat{\mathbf{v}}_{\mathrm{n}}^{2} \\ \vdots \\ \widehat{\mathbf{v}}_{\mathrm{n}}^{j} \end{bmatrix} \quad (1)$$

where $\boldsymbol{O}_{ij}=\exp(-\boldsymbol{d}_{ij}^{2}/\boldsymbol{D}_{i}^{2})$; $\mathbf{v}_{\mathrm{e}}^{i}$ and $\mathbf{v}_{\mathrm{n}}^{i}$ are east and north components of velocities at the ith GPS station; $\boldsymbol{d}_{ij}$ is the distance between the ith GPS station and the jth node; D_i is a spatial length and controls the size of interpolation window. We search for minimum D_i at each GPS station to ensure it is located inside the convex hull composed by

Table 1
Station velocity with respect to Paisha, Penghu (S01R) on two sides of the Longitudinal Valley fault (LVF)

Station	Longitude (°)	Latitude (°)	*V* (mm/yr)	*Azi* (°)	*a* (mm/yr)	*b* (mm/yr)	Azi_a (°)	*n*	Time span
Sites to the west of the LVF									
0054	121.1989	23.1286	32.8	298	0.5	0.4	86	8	1993.4–1999.4
0107	120.8442	24.4444	6.3	291	0.3	0.3	85	7	1993.5–1999.6
0131	121.5431	23.9636	19.0	308	0.3	0.3	85	11	1993.4–1999.6
0135	121.3486	23.2908	55.8	317	0.5	0.4	78	8	1993.4–1999.4
0201	121.3200	23.3539	32.8	302	0.9	0.9	67	7	1994.2–1999.4
0206	121.1092	22.8100	45.1	279	0.5	0.5	86	7	1993.4–1999.4
0207	121.1475	22.8178	58.6	303	0.6	0.6	70	6	1993.4–1998.3
0211	121.1419	22.7533	40.9	287	0.5	0.4	91	9	1993.4–1999.4
0216	121.6308	24.0228	14.3	313	0.4	0.3	79	10	1993.4–1999.4
0241	121.3347	23.3361	52.0	310	0.9	0.9	45	6	1994.2–1999.4
0242	121.3250	23.2961	58.3	317	1.4	1.3	45	5	1995.2–1999.4
0283	121.2336	23.1178	64.1	311	0.6	0.6	75	6	1993.4–1998.3
0437	120.4675	23.2369	21.2	275	0.9	0.8	92	6	1993.4–1998.5
0504	121.6975	24.7311	8.3	131	0.3	0.3	86	6	1993.5–1999.6
0505	121.7569	24.7464	11.7	136	0.4	0.4	99	7	1994.9–1999.6
0544	120.6333	22.7828	50.2	268	0.6	0.5	103	7	1995.3–1999.4
0575	120.6639	22.4139	52.7	269	2.3	2.1	94	3	1997.1–1999.4
0621	120.4339	22.7897	48.7	258	0.4	0.3	95	11	1993.4–1999.0
0727	121.3925	23.6056	30.3	298	0.4	0.4	80	9	1993.4–1999.4
0801	121.4936	25.2122	2.2	180	0.4	0.4	116	7	1993.2–1998.9
0971	121.6958	24.6633	16.7	113	0.4	0.3	85	8	1994.9–1999.6
0980	121.1714	24.8889	1.0	249	0.4	0.3	77	9	1993.5–1999.6
0982	121.4575	25.1133	4.8	129	0.4	0.4	91	6	1993.2–1998.9
0991	121.3306	25.0167	1.3	233	0.5	0.5	74	9	1993.2–1998.9
0996	121.8017	24.8706	5.7	167	0.3	0.3	82	10	1993.5–1999.6
1043	121.5486	24.9925	2.2	87	1.1	1.0	109	5	1993.2–1997.9
1045	121.6075	25.1292	4.4	137	0.4	0.4	88	7	1993.2–1998.9
1055	121.6992	25.1089	3.7	147	0.5	0.5	83	6	1993.2–1998.9
1063	121.6700	25.1775	4.4	139	0.4	0.4	79	6	1993.2–1998.9
1064	121.5292	25.0842	1.9	127	0.4	0.3	83	7	1993.2–1998.9
1102	121.4778	25.1442	1.5	132	0.8	0.7	144	4	1995.3–1998.9
1119	121.6039	25.2528	2.6	143	0.5	0.5	39	6	1993.2–1998.9
1139	121.7442	24.8050	9.1	140	0.4	0.4	90	7	1993.5–1999.6
1168	121.7756	25.1431	5.2	124	0.5	0.4	76	9	1993.2–1998.9
1172	121.3156	23.2858	54.2	311	1.7	1.5	1	4	1995.2–1999.4
1178	121.2825	23.2911	29.6	302	1.6	1.6	132	4	1995.2–1999.4
1215	121.5869	23.8878	28.0	316	0.4	0.4	70	8	1993.4–1999.4
13R3	121.3247	23.3144	41.8	306	1.7	1.5	37	5	1995.2–1999.4
13R4	121.2989	23.3017	33.0	302	1.5	1.4	34	4	1995.2–1999.4
1449	121.4044	24.0203	17.4	328	1.9	1.8	96	6	1994.2–1999.6
5936	121.1267	24.0131	22.7	295	0.3	0.2	81	10	1993.5–1999.6
6267	121.3953	24.6844	2.9	330	0.3	0.3	83	7	1994.9–1999.6
6389	121.2847	24.1525	22.2	321	0.3	0.2	85	9	1993.5–1999.6
6636	120.6519	22.5822	50.6	272	0.6	0.6	112	5	1995.3–1999.4
7205	120.7656	23.0750	44.4	271	0.4	0.3	90	14	1993.4–1999.4
8046	121.1764	23.0825	33.8	294	0.6	0.5	88	7	1993.4–1999.4
8152	121.4872	23.6453	48.3	316	1.5	1.2	82	5	1996.1–1999.4
A247	120.4078	24.0206	4.2	276	0.3	0.3	76	7	1993.5–1999.6
C006	120.5367	23.0775	37.3	271	0.7	0.6	114	3	1996.1–1999.0
CHNL	120.5633	23.3772	22.8	241	0.9	0.9	112	8	1997.9–1999.0
CHSN	121.5533	25.1708	2.4	140	0.4	0.4	108	7	1993.2–1998.9
CK01	120.2106	22.9758	14.5	260	0.2	0.2	73	16	1994.1–1999.6
CKLS	121.8656	25.0931	3.0	138	0.4	0.3	73	10	1993.5–1999.6
CPUL	120.6347	23.9275	6.0	287	0.3	0.3	75	10	1993.5–1999.6
FCWS	121.2497	24.8506	2.0	288	0.2	0.1	80	21	1993.5–1999.6
FLNM	121.4533	23.7464	25.8	307	0.2	0.1	92	24	1994.1–1999.6
FONS	120.3817	22.5300	47.4	246	0.5	0.4	87	11	1993.4–1999.4
G013	120.5511	22.4714	48.7	265	2.6	2.4	95	3	1997.1–1999.4
G017	120.5983	22.8272	56.1	265	1.7	1.7	101	4	1997.1–1999.0
G023	120.4686	22.6147	52.7	266	2.6	2.4	95	4	1997.1–1999.4
HTZS	120.9819	23.9739	18.2	291	0.3	0.2	81	9	1993.5–1999.6
I001	121.4789	24.9967	2.1	158	0.4	0.4	78	6	1993.2–1998.9
I004	120.2392	22.9736	11.7	249	0.6	0.5	89	10	1993.4–1998.0
I007	120.7744	23.7561	14.4	292	0.3	0.2	76	15	1993.4–1999.6
I029	121.8167	24.7678	13.0	138	0.3	0.3	81	7	1993.5–1999.6
I042	120.2528	22.7700	22.6	259	0.3	0.3	108	11	1993.4–1999.6
I045	120.3275	22.6675	48.7	246	0.4	0.4	105	11	1993.4–1999.4
I301	121.7717	24.6839	20.7	123	0.4	0.4	100	6	1994.9–1999.6
JFES	120.8417	23.9344	15.1	294	0.4	0.3	76	8	1993.5–1999.6
KDNM	120.7819	21.9494	36.3	277	0.2	0.2	100	22	1994.1–1999.6
KLUN	121.3842	24.9958	0.9	247	0.3	0.3	70	14	1993.2–1999.6
KUYN	121.0761	25.0375	2.5	154	0.4	0.4	89	7	1993.5–1999.6
LIUC	120.3786	22.3408	48.3	241	0.6	0.5	77	8	1993.4–1999.4

(continued on next page)

Table 1 (*continued*)

Station	Longitude (°)	Latitude (°)	*V* (mm/yr)	*Azi* (°)	*a* (mm/yr)	*b* (mm/yr)	Azi_a (°)	*n*	Time span
Sites to the west of the LVF									
MERK	120.3094	23.7975	1.6	215	0.3	0.3	79	14	1993.4–1999.6
N091	121.2522	25.0014	2.5	169	0.5	0.4	102	6	1995.3–1999.6
NCTU	120.9972	24.7889	4.5	321	0.3	0.3	95	14	1995.9–1999.6
P049	121.5808	25.1656	3.8	116	0.8	0.8	143	5	1993.2–1997.9
PKGM	120.3056	23.5800	7.7	327	0.2	0.2	95	17	1995.2–1999.6
S002	119.4386	23.2133	0.2	191	0.4	0.3	99	6	1993.4–1999.6
S003	120.1628	23.1731	2.5	252	0.4	0.3	108	11	1993.4–1999.0
S004	120.1886	23.3825	3.4	303	0.4	0.3	77	8	1993.4–1998.6
S005	120.2167	23.5992	2.4	80	0.5	0.4	79	7	1993.4–1998.6
S007	120.3831	23.2542	13.0	277	0.5	0.4	81	7	1993.4–1998.6
S008	120.4436	23.4200	11.3	287	0.5	0.5	79	7	1993.4–1998.6
S011	120.3394	23.2056	10.5	286	0.2	0.2	87	12	1993.4–1999.6
S012	120.4883	23.0594	33.2	270	0.2	0.2	97	12	1993.4–1999.6
S013	120.5636	23.2536	27.6	280	0.4	0.4	84	7	1993.4–1998.6
S014	120.6489	23.4044	22.7	273	0.4	0.4	92	8	1993.4–1998.6
S015	120.6814	23.5550	15.8	294	0.5	0.4	90	8	1993.4–1998.6
S016	120.8028	24.1794	9.2	286	0.3	0.2	79	8	1993.5–1999.6
S017	120.7644	24.6011	3.6	297	0.4	0.3	92	9	1993.5–1999.6
S018	121.0003	24.8833	2.6	228	0.3	0.3	87	9	1993.5–1999.6
S019	121.2914	25.1022	2.6	215	0.4	0.4	42	10	1993.2–1999.6
S01R	119.5925	23.6553	0.0	91	0.0	0.0	180	30	1993.2–1999.6
S020	121.5122	25.2853	2.5	201	0.4	0.4	84	8	1993.2–1998.9
S021	120.7131	21.9950	44.6	266	0.7	0.6	104	6	1993.4–1999.4
S022	120.6239	22.3664	48.6	268	0.5	0.4	87	7	1993.4–1999.4
S024	120.7036	22.9156	51.5	269	0.4	0.3	54	8	1993.4–1998.2
S025	120.8244	23.2636	30.8	275	0.5	0.5	83	7	1993.4–1998.5
S026	120.9164	23.2822	32.3	280	0.4	0.4	84	9	1993.4–1998.5
S027	120.8894	23.4839	28.2	282	0.3	0.3	85	15	1993.4–1999.4
S028	121.1425	23.7517	26.7	295	0.6	0.4	100	8	1994.2–1999.6
S029	121.5181	25.1272	2.0	165	0.4	0.4	95	7	1993.2–1998.9
S030	121.0275	24.2806	9.3	300	0.7	0.6	81	6	1993.5–1998.5
S031	121.3081	24.3378	10.0	321	0.3	0.3	82	10	1993.5–1999.6
S032	121.1139	24.5064	14.1	303	0.3	0.2	79	9	1993.5–1999.6
S033	121.2800	23.1031	63.5	312	0.5	0.4	84	7	1993.4–1999.4
S034	121.7742	24.8647	7.6	122	0.7	0.7	68	5	1996.3–1999.6
S035	121.9994	25.0056	4.8	156	0.3	0.3	72	10	1993.5–1999.6
S039	121.2758	23.2764	31.5	302	0.4	0.3	89	9	1993.4–1999.4
Sites to the west of the LVF									
S040	121.1500	23.0306	33.5	292	0.4	0.4	85	8	1993.4–1999.4
S041	120.8489	21.9261	35.9	286	0.7	0.7	116	7	1993.4–1999.4
S042	120.8550	22.2419	42.4	281	0.5	0.4	98	10	1993.4–1999.4
S043	120.9350	22.4717	37.4	286	0.4	0.4	95	8	1993.4–1999.4
S044	121.0225	22.6778	31.2	281	0.4	0.4	92	11	1993.4–1999.4
S045	121.0806	22.8803	31.4	289	0.4	0.4	89	8	1993.4–1999.4
S046	121.0550	23.1472	31.3	292	0.4	0.4	87	8	1993.4–1999.4
S047	121.3594	23.4708	34.0	307	0.4	0.3	89	13	1993.4–1999.4
S048	121.4050	23.7094	24.6	299	0.3	0.3	82	14	1993.4–1999.6
S049	121.5406	23.8867	23.0	303	0.3	0.3	83	13	1993.4–1999.6
S050	121.6625	24.1453	7.8	278	0.3	0.3	88	12	1993.4–1999.6
S052	121.8678	24.5939	37.9	149	0.4	0.3	95	9	1994.9–1999.6
S053	121.7781	24.3972	22.9	140	0.4	0.4	105	9	1994.9–1999.6
S054	121.1975	22.7939	63.6	307	0.5	0.4	95	7	1993.4–1999.4
S055	121.1228	23.1342	32.1	293	0.6	0.5	90	7	1993.4–1999.4
S056	121.1986	23.0369	62.5	306	0.5	0.4	83	7	1993.4–1999.4
S057	121.3092	22.9731	65.8	309	0.4	0.4	90	7	1993.4–1999.4
S058	121.4544	23.3194	64.6	316	0.2	0.2	91	21	1993.4–1999.4
S059	121.5133	23.4883	66.3	315	0.5	0.5	79	7	1993.4–1999.4
S061	121.5589	23.7511	33.6	325	0.4	0.4	78	7	1993.4–1999.4
S064	120.5039	22.9486	47.1	270	0.6	0.5	88	9	1993.4–1998.0
S065	120.6111	23.1200	37.3	276	0.4	0.4	82	10	1993.4–1999.4
S066	120.5117	23.1922	29.9	277	0.6	0.5	79	7	1993.4–1998.5
S067	120.3839	22.9514	25.0	255	0.4	0.4	110	7	1993.4–1999.0
S068	120.3664	23.0853	10.8	254	0.8	0.7	126	5	1993.4–1999.0
S069	120.5011	23.3264	23.5	277	0.6	0.5	78	7	1993.4–1998.6
S070	120.5619	23.4519	16.1	282	0.4	0.4	82	9	1993.4–1998.6
S071	120.3219	23.4694	4.9	276	0.4	0.4	79	7	1993.4–1998.6
S072	121.1625	22.9256	63.7	305	0.5	0.4	79	7	1993.4–1999.4
S073	121.2881	23.2397	55.6	307	0.4	0.4	88	8	1993.4–1999.4
S074	121.4953	23.7158	34.5	322	0.4	0.3	77	8	1993.4–1999.4
S075	121.5283	23.8275	26.5	313	0.5	0.4	70	6	1993.4–1999.4
S077	121.5250	23.5964	62.0	317	0.5	0.4	71	7	1993.4–1999.4
S078	121.0453	23.1669	31.0	287	0.6	0.5	81	5	1993.4–1999.4
S079	121.0269	23.2011	29.1	281	0.9	0.8	69	5	1993.4–1998.3
S080	121.0131	23.2203	31.3	286	0.5	0.5	82	9	1993.4–1998.3
S082	120.3686	23.2353	11.3	275	1.4	1.1	61	6	1993.4–1998.5

Table 1 (*continued*)

Station	Longitude (°)	Latitude (°)	*V* (mm/yr)	*Azi* (°)	*a* (mm/yr)	*b* (mm/yr)	*Azi*$_{\mathrm{a}}$ (°)	*n*	Time span
Sites to the west of the LVF									
S083	120.3892	23.2367	15.8	264	1.5	1.3	67	6	1993.4–1998.5
S085	120.4156	23.2356	15.6	259	1.1	0.9	72	6	1993.4–1998.5
S087	120.4486	23.2358	15.6	274	1.1	1.0	96	6	1993.4–1998.5
S088	120.4592	23.2403	20.2	279	1.0	0.9	85	6	1993.4–1998.5
S089	120.4675	23.2211	20.0	275	0.9	0.9	84	6	1993.4–1998.5
S090	120.4806	23.2094	24.5	269	0.9	0.9	87	6	1993.4–1998.5
S091	120.4942	23.2047	30.0	277	1.2	1.1	121	6	1993.4–1998.5
S092	120.5286	23.1850	29.9	279	0.4	0.3	107	11	1993.4–1999.6
S093	121.6267	24.0147	14.6	311	0.4	0.3	86	8	1993.4–1999.6
S094	120.5014	23.6606	5.4	307	0.4	0.3	80	11	1993.4–1998.6
S095	121.6511	25.2292	4.5	154	1.3	1.2	123	4	1996.3–1998.9
S096	120.3383	22.7703	45.6	258	1.7	1.6	119	5	1996.1–1999.6
S097	120.3864	22.7756	45.7	252	1.2	1.1	99	5	1996.1–1999.0
S098	121.4344	23.6242	44.9	305	1.1	1.1	94	4	1996.5–1999.4
S099	121.4914	23.6339	47.7	313	0.9	0.9	67	4	1996.5–1999.4
S100	121.5008	23.5808	58.2	316	2.5	2.2	99	3	1997.1–1999.4
S101	121.6139	25.0406	6.1	164	0.1	0.1	72	24	1993.2–1999.6
S103	120.4753	23.5644	7.7	290	0.2	0.1	93	23	1993.4–1999.4
S104	121.1894	22.8208	62.3	309	0.2	0.1	95	24	1993.4–1999.6
S105	121.1128	22.9517	33.2	292	0.2	0.2	90	21	1993.4–1999.6
S122	121.4028	23.5783	37.4	301	1.2	1.1	92	4	1996.5–1999.4
S124	121.5353	24.4981	10.1	69	0.9	0.8	112	4	1996.5–1999.6
S125	120.7525	22.4058	48.0	273	2.3	2.1	96	3	1997.1–1999.4
S130	120.7433	22.7444	51.0	275	1.7	1.6	96	5	1997.1–1999.4
S23R	120.6061	22.6450	51.3	270	0.1	0.1	103	28	1993.2–1999.6
S291	120.3125	23.3383	8.9	257	1.2	1.1	93	6	1995.3–1998.6
S411	121.4008	25.1172	1.6	200	0.4	0.4	87	8	1993.2–1998.9
S412	121.4575	25.0775	1.7	166	0.4	0.4	65	8	1993.2–1998.9
S413	121.5797	24.9719	3.1	119	0.3	0.3	74	12	1993.2–1999.6
SANT	121.4164	23.1250	66.5	311	0.4	0.4	90	8	1993.4–1999.4
STCS	120.4808	23.5358	10.8	278	0.5	0.5	72	7	1993.4–1998.6
TAIW	121.5367	25.0214	2.7	86	0.1	0.1	72	20	1993.2–1998.9
TAPN	121.6356	25.0231	5.9	110	0.3	0.3	84	14	1993.2–1999.6
TECS	120.6550	24.3564	5.0	284	0.4	0.3	87	8	1994.9–1999.6
TFLS	121.0500	24.6806	4.5	324	0.3	0.3	80	10	1993.5–1999.6
TMLM	121.0075	22.6161	32.2	285	0.2	0.2	102	19	1995.2–1999.6
WK5A	121.4458	25.0692	0.6	86	2.4	2.0	84	4	1994.3–1998.9
WNTS	120.5844	24.1381	4.8	276	0.3	0.2	82	9	1993.5–1999.6
YMSM	121.5742	25.1658	2.3	118	0.2	0.2	81	22	1994.1–1999.6
Sites to the east of the LVF									
0135	121.3486	23.2908	55.8	317	0.5	0.4	78	8	1993.4–1999.4
0207	121.1475	22.8178	58.6	303	0.6	0.6	70	6	1993.4–1998.3
0241	121.3347	23.3361	52.0	310	0.9	0.9	45	6	1994.2–1999.4
0242	121.3250	23.2961	58.3	317	1.4	1.3	45	5	1995.2–1999.4
0283	121.2336	23.1178	64.1	311	0.6	0.6	75	6	1993.4–1998.3
1215	121.5869	23.8878	28.0	316	0.4	0.4	70	8	1993.4–1999.4
8152	121.4872	23.6453	48.3	316	1.5	1.2	82	5	1996.1–1999.4
S033	121.2800	23.1031	63.5	312	0.5	0.4	84	7	1993.4–1999.4
S054	121.1975	22.7939	63.6	307	0.5	0.4	95	7	1993.4–1999.4
S056	121.1986	23.0369	62.5	306	0.5	0.4	83	7	1993.4–1999.4
S057	121.3092	22.9731	65.8	309	0.4	0.4	90	7	1993.4–1999.4
S058	121.4544	23.3194	64.6	316	0.2	0.2	91	21	1993.4–1999.4
S059	121.5133	23.4883	66.3	315	0.5	0.5	79	7	1993.4–1999.4
S061	121.5589	23.7511	33.6	325	0.4	0.4	78	7	1993.4–1999.4
S063	121.4786	22.6647	79.6	305	0.4	0.4	97	8	1993.4–1999.4
S072	121.1625	22.9256	63.7	305	0.5	0.4	79	7	1993.4–1999.4
S073	121.2881	23.2397	55.6	307	0.4	0.4	88	8	1993.4–1999.4
S074	121.4953	23.7158	34.5	322	0.4	0.3	77	8	1993.4–1999.4
S075	121.5283	23.8275	26.5	313	0.5	0.4	70	6	1993.4–1999.4
S077	121.5250	23.5964	62.0	317	0.5	0.4	71	7	1993.4–1999.4
S098	121.4344	23.6242	44.9	305	1.1	1.1	94	4	1996.5–1999.4
S099	121.4914	23.6339	47.7	313	0.9	0.9	67	4	1996.5–1999.4
S100	121.5008	23.5808	58.2	316	2.5	2.2	99	3	1997.1–1999.4
S102	121.5581	22.0372	81.5	302	0.3	0.2	105	14	1993.2–1996.5
S104	121.1894	22.8208	62.3	309	0.2	0.1	95	24	1993.4–1999.6
SANT	121.4164	23.1250	66.5	311	0.4	0.4	90	8	1993.4–1999.4

V is the station velocity; *Azi* is the azimuth of *V*; *a*, *b* are the semi-major and semi-minor axes for error ellipse of *V*; *Azi*$_{\mathrm{a}}$ is the azimuth of *a*; *n* is number of survey.

nodes (the size of D_i is about 30–40 km); $\hat{\mathbf{v}}_{\mathrm{e}}^{l}$ and $\hat{\mathbf{v}}_{\mathrm{n}}^{l}$ are estimated north and east component at the *j*th point. Eq. (1) can be written as:

$$\mathbf{d} = \mathbf{G}\mathbf{m} \tag{2}$$

where ***d*** is a matrix of observed GPS velocities, ***G*** is a matrix of Green's functions related to the distance between each GPS station and node, and ***m*** is the desired velocity field. To ensure that the velocity varies smoothly in space and to balance the representative area associated with individual data points, we augment Eq. (2) to be:

$$\begin{bmatrix} \mathbf{W}\mathbf{d} \\ 0 \end{bmatrix} = \begin{bmatrix} \mathbf{W}\mathbf{G} \\ \alpha\nabla^2 \end{bmatrix}\mathbf{m} \tag{3}$$

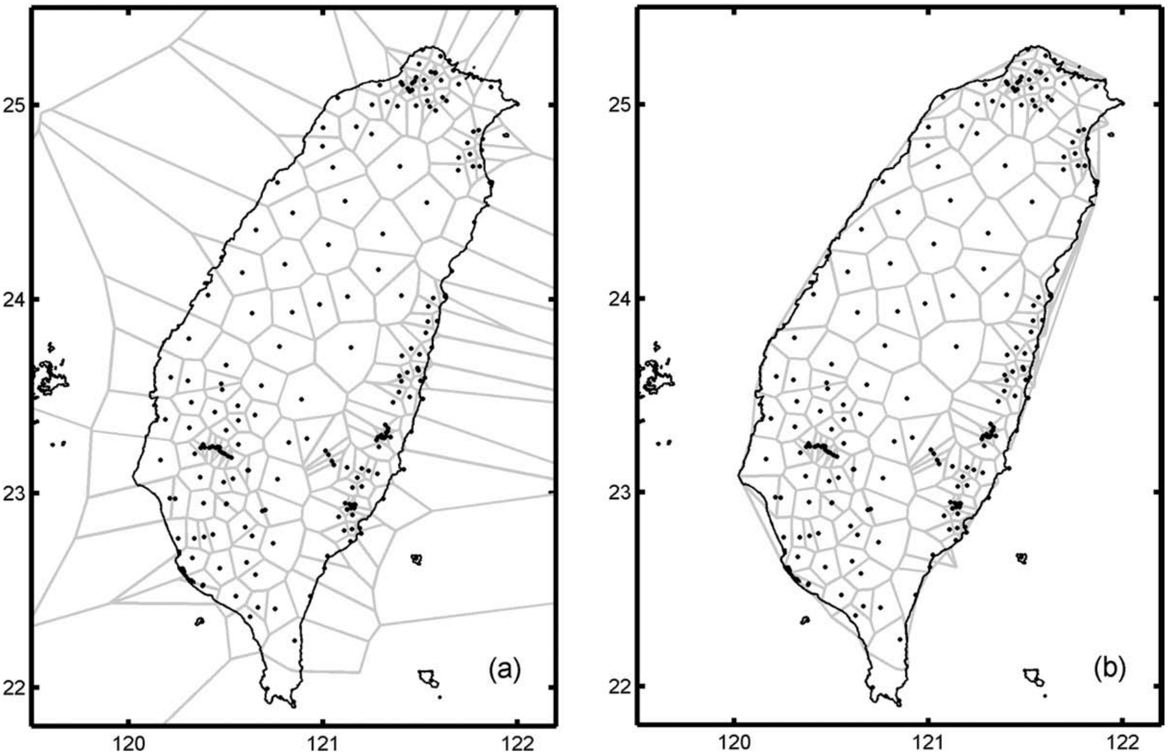

Fig. 3. The Voronoi diagram associated with the distribution of GPS sites used in this study. (a) The Voronoi cell (polygon) associated with each site indicates the region represented by that particular site. (b) The Voronoi diagram modified to remove extension of the cells off shore.

where ∇^2 is the smoothing matrix using the finite difference approximation of the Laplacian operator; and α serves as the weighting of the model roughness versus data misfit. We choose the value of α by cross-validation (Matthews and Segall, 1993). In order to take account the variable contributions from individual data, we weighted each observation with two types of weighting, including the observational error ($\boldsymbol{W}_\mathrm{s}$) and the station density ($\boldsymbol{W}_\mathrm{a}$), each one equally contributes to the inversion. The weighting matrix, $\boldsymbol{W}$, equals to the multiple of $\boldsymbol{W}_\mathrm{s}$ and $\boldsymbol{W}_\mathrm{a}$; where $\boldsymbol{W}_\mathrm{s}$ is the reciprocal of observation error, $\boldsymbol{W}_\mathrm{a}$ is estimated from the area of the Voronoi cells associated with the geodetic network. The GPS site associated with a given Voronoi cell will be the closest site to any point in that cell. Thus the area of cell represents a good metric for the area that a given site should represent. The Voronoi cells for our data set are given in Fig. 3a. Voronoi vertices located offshore are replaced by the closest point on land (Fig. 3b). In addition, we assign a maximum area weighting for several sites located on offshore islands such as Penghu, Luato and Lanhsu. The actual value $\boldsymbol{W}_\mathrm{a}$ corresponds to the square root of cell area associated with a given GPS station. Using $\boldsymbol{W}_\mathrm{a}$ has the effect of stabilizing the inversion and avoids biased information from irregularly station geometry, such that dense pockets of stations do not dominate results. The modeling velocity and residuals are shown in Fig. 4a, b. The strain rate at each node is determined by taking spatial derivatives of modeling velocities, with fully propagated covariance matrix from observed GPS velocities to estimated strain rates (Fig. 4c). Note that the large misfit in modeling velocity in the SW Taiwan and the Longitudinal Valley is possibly associated with fault creep near the surface (Fig. 4b). The sharp velocity discontinuity corresponding to the fault creep at shallow depths cannot be reproduced in our method.

4. Surface strain rates and crustal stress

Earlier studies (Bos et al., 2003; Chang et al., 2003) adopt different methods to estimate the strain-rate filed in Taiwan using GPS velocity between 1990 and 1995 (Yu et al., 1997). Chang et al. (2003) do not consider the GPS velocity errors and the distribution of GPS stations. Bos et al. (2003) describe the surface deformation in terms of the continuous deformation and discrete movements along faults; requiring a priori knowledge of fault geometries. To illustrate the relationship between strain rate and stress in the Taiwan plate boundary zone, we first use the aforementioned method to compute the strain rate field from GPS data between 1993 and 1999 (Fig. 4c) and then compare principal strain-rate axes with stress axes derived from stress tensor inversions. The one standard deviation of dilatation rate is shown in Fig. 4d. The errors are normally around 0.1 µstrain/yr over most of Taiwan and no more than 0.3 µstrain/yr at the southern and northern tips. The inferred dilatation rates in most areas are larger than their errors.

4.1. The strain-rate field derived from GPS data

Strain rates computed from GPS velocities indicate SW Taiwan and the Longitudinal Valley in eastern Taiwan are experiencing high NW to W–SE to E contraction with the maximum rates more than 1 µstrain/yr (Fig. 4c). The trends of inferred maximum principal contraction axes in western Taiwan, from north to south, are ~N40°W in the Hsinchu area, ~N70°W in the Taichung area and ~N80°W in the Tainan–Kaohsiung area. In the Longitudinal Valley of eastern Taiwan, the maximum contraction axis counterclockwise rotates from N30°W in the Hualien area to N60°W in the Taitung area. The general trends of contraction axes

Fig. 4. (a) Observed and interpolated GPS velocities shown as black and red vectors, respectively; (b) Residual velocities after removal of the interpolated field; (c) Dilatation and principal strain rates. The color scale indicates dilatation rate in µstrian/yr. Black (contraction) and grey (extension) vectors denote the two principal strain-rate axes. Major faults are indicated as green lines. The star denotes the epicenter of 1999 Chi-Chi earthquake. (d) One standard deviation in µstrian/yr for the dilatation rate. The base of foreland basin is indicated in red contours at intervals of 1 km (Lin and Watts, 2002). The azimuths of maximum contractional strain-rate axes are shown in grey contours at intervals of 20°. Note that the azimuth counts from the north, counterclockwise is negative.

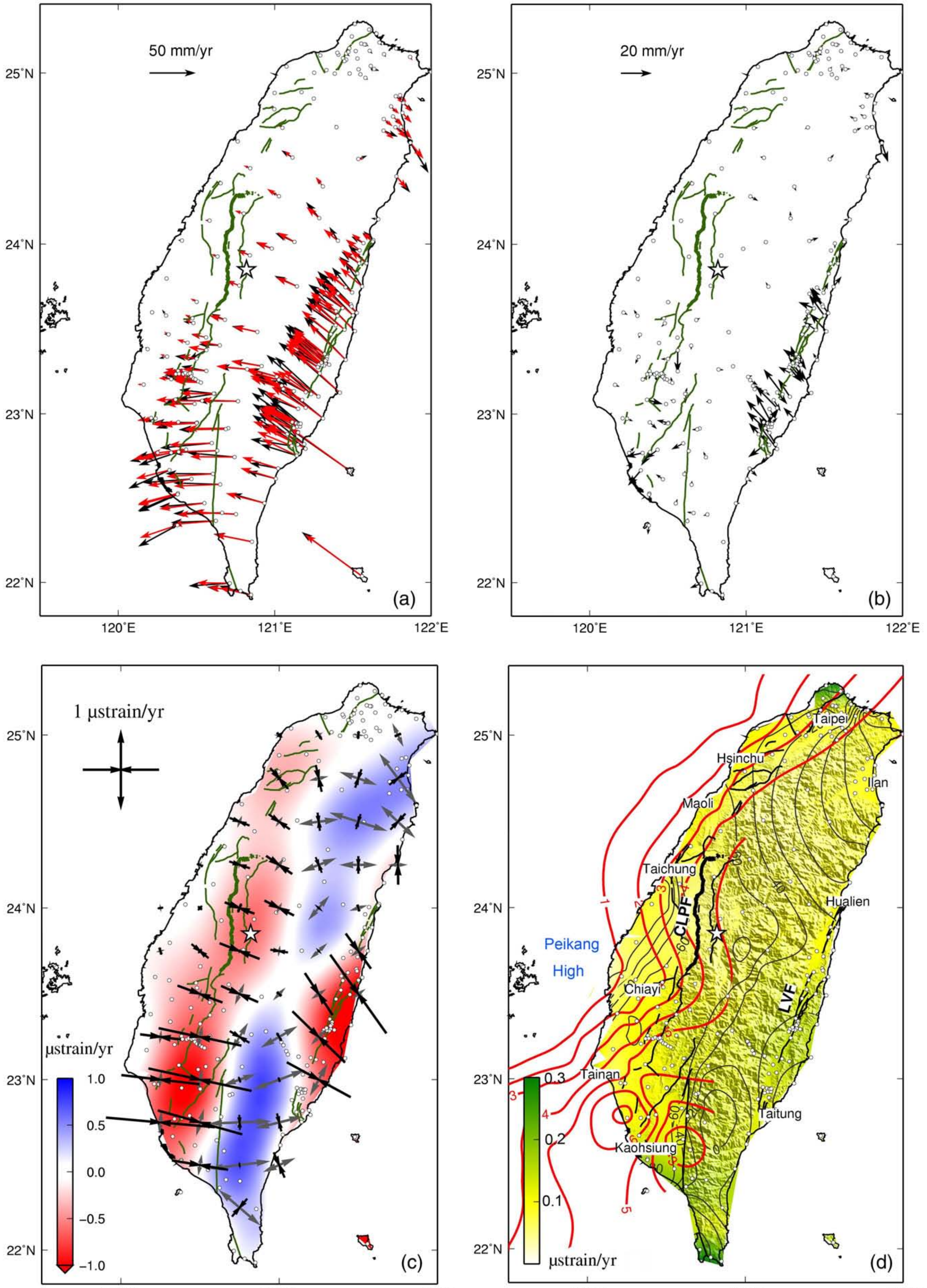
50 mm/yr
25°N
24°N
23°N
22°N
120°E
121°E
122°E
(a)
20 mm/yr
(b)
1 μstrain/yr
μstrain/yr
1.0
0.5
0.0
−0.5
−1.0
(c)
Taipei
Hsinchu
Ilan
Maoli
Taichung
Hualien
Peikang
High
CLPF
LVF
Chiayi
Tainan
Kaohsiung
Taitung
0.3
0.2
0.1
μstrain/yr
1
2
3
4
5
6
(d)

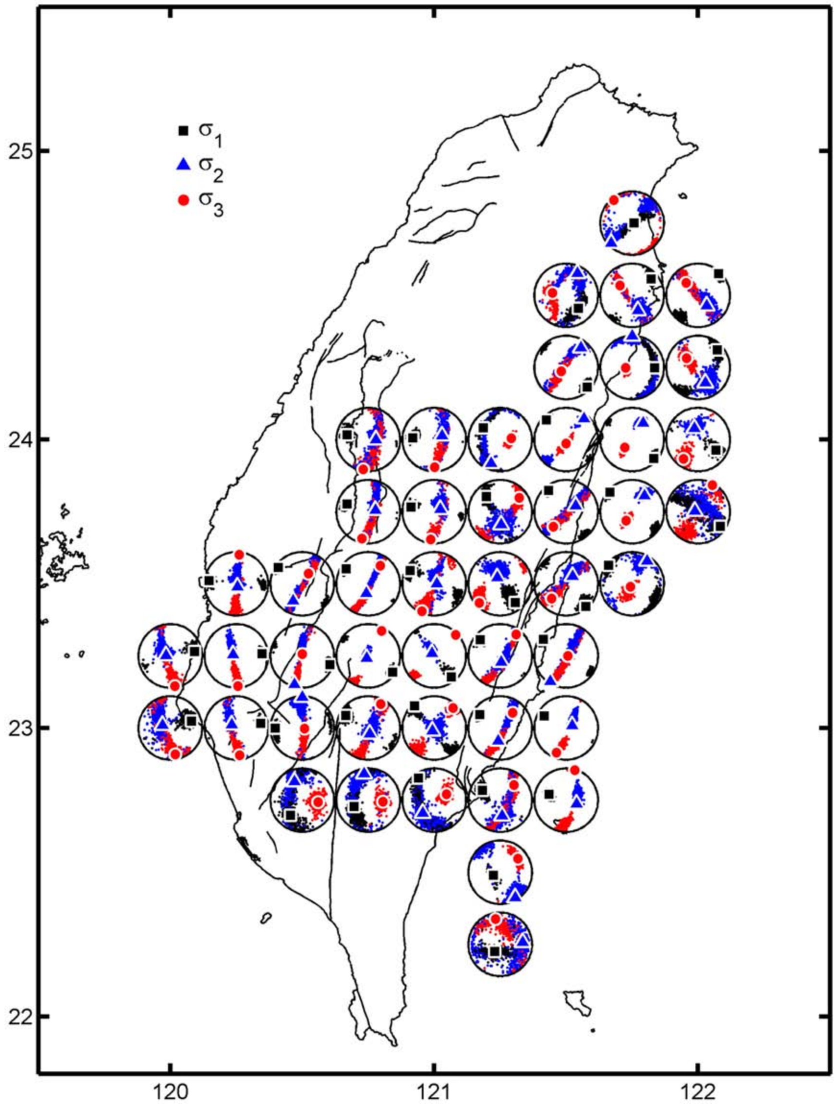

Fig. 5. Results of the stress tensor inversions. Squares, triangles, and circles represent three principal stress axes, σ_1, σ_2 and σ_3, in equal-area projection of the lower hemisphere. The best solution is marked by large symbols with white outlines. The small symbols show the distribution of stress axes within 95% confidence region.

are consistent with previous results based on different approaches (Bos et al., 2003; Chang et al., 2003).

In contrast to the contraction regime in western Taiwan and the Longitudinal Valley, northeastern Taiwan and the Central Range show significant extension. The trends of extension axes vary from north to south: they are NW–SE-directed in the Ilan plain, NE–SW-directed near the middle part of the Central Range, and NEE–SWW-directed in the southern Central Range. In northeastern Taiwan, orientations of extension axes show a counterclockwise rotation between offshore Ilan (N40°W) to inland area (N70°W) near 121.5°E, 24.5°N. On the other hand, subtle NE–SW and significant NEE–SWW directed extensions are derived from our model near the middle (~24°N) and southern portions (22°N–23.5°N) of the Central Range, respectively. The first-order pattern of the trend of extension axes corresponds to the results in previous studies (Bos et al., 2003; Chang et al., 2003).

4.2. Principal stress axes derived from stress tensor inversions

The GPS velocities image the surface strain rate, while earthquake focal mechanisms demonstrate the state of stress in the seismogenic crust. In order to tell how strain or stress varies with depth, we examine the stress regime in the crust using earthquake focal mechanisms with depths less than 30 km. We use focal mechanism determining by first-motion polarities of P waves from Wu et al. (2008). They implement a genetic algorithm in a non-linear global search to find the best earthquake focal mechanism with $M_L > 4$ between 1991 and 2005. In this study, we only use the data before the Chi-Chi earthquake (1991–1999.7). Alternatively, we could use the earthquake focal mechanisms determined from the modeling of waveforms recorded by the Broadband Array in Taiwan for Seismology (BATS); however, the number of shallow earthquakes (Kao and Jian, 2001) is not sufficient for a stress tensor inversion.

We use the algorithm from Michael (1984, 1987) to find the stress tensor that minimizes the difference between the shear stress on the fault plane and the fault slip rake. In order to find a continuous variation of stress orientations in space, we use a moving-window inversion on the 0.25°-spacing grid and include all events within a $0.5^\circ \times 0.5^\circ$ rectangle centered at the node. We estimate the stress tensor only when there are at least 10 earthquakes within a given rectangular box (Fig. 5). The resulting maximum and minimum stress axes projected to the surface are shown in Fig. 6. The length of stress

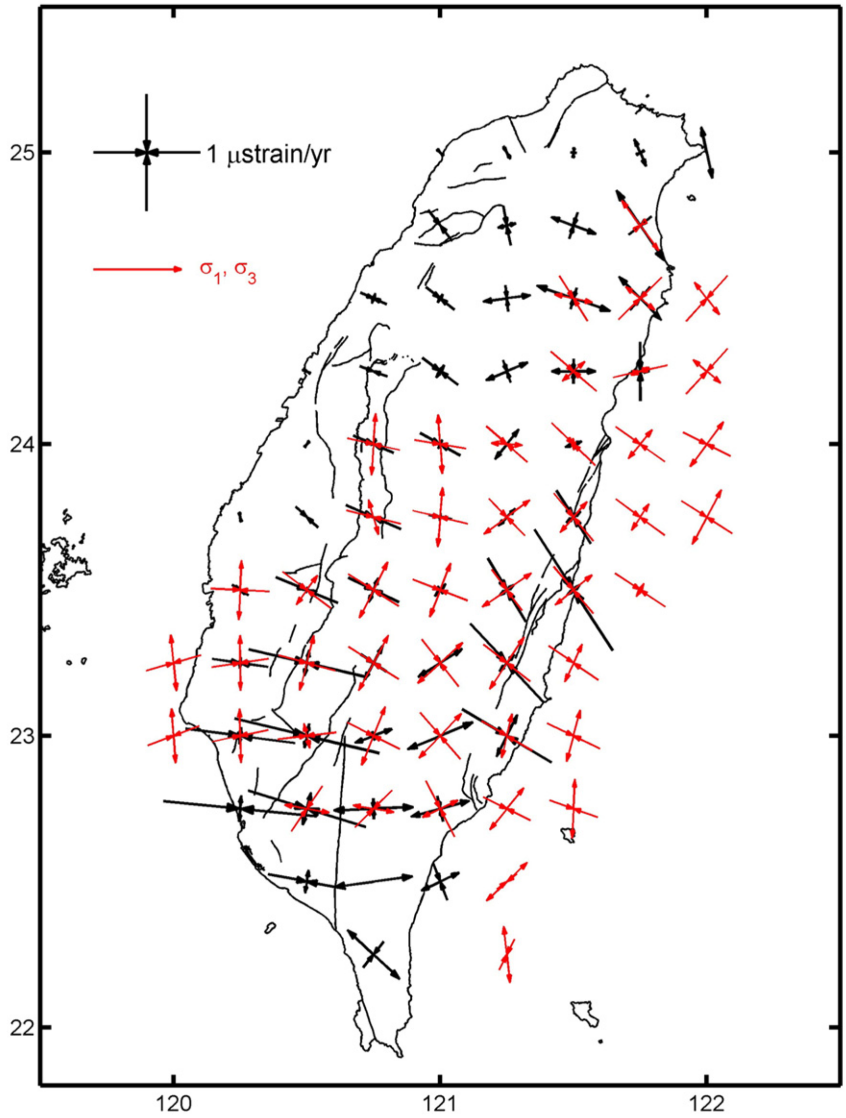

Fig. 6. The principal strain-rate (black) and stress (red) axes. Surface projections of the σ_1 and σ_3 axes are the largest when the plunges are 0° (horizontal) and are close to 0 when the plunges are 90° (vertical).

axis is the largest when the plunge is 0° (horizontal) and is close to 0 when the plunge is 90° (vertical). While we attempt to use an adequate number of focal mechanisms to constrain the stress field, we are hampered by a limited understanding of the error in the input focal mechanisms. To estimate the quality of stress tensor inversion, we use bootstrap method re-sampling actual focal mechanisms to generate 500 synthetic data sets and then computing the 95% confidence region of principal stress axes (Fig. 5). We find the trend of maximum principal stress axis, σ_1, is the most reliable axis among three and the plunge is close to horizontal, consistent with the compressive stress regime dominant in the Taiwan collision zone. The intermediate and minimum stress axes (σ_2 and σ_3) vary a lot in most regions. Therefore, we only discuss the trend of stress axis, σ_1, and the maximum principal strain-rate axis in the next section.

The ratio of principal stress difference $\phi = \frac{\sigma_2 - \sigma_3}{\sigma_1 - \sigma_3}$ from the stress tensor inversion is shown in Fig. 7. If $\sigma_1 = \sigma_2$, namely $\phi = 1$, the stress status of the crust corresponds to a stress regime transitional to normal faulting; while if $\sigma_2 = \sigma_3$, namely $\phi = 0$, corresponds to a stress regime to thrust faulting. For the value of ϕ close to 0 or 1, represents the near-transitional stress regime that requires only minor fluctuations in stress magnitude to change from one stress regime to the other.

4.3. Comparison of orientations between strain-rate and stress axes and its implication

To illustrate the variation of faulting type from surface to the crust, we compare the trends of principal strain rates derived from GPS velocity field and principal stress axes derived from earthquake focal mechanisms with depths less than 30 km. In Fig. 6, we find that the orientations of principal strain-rate and stress axes generally agree. This implies that a large scale variation of stress orientations from the surface to the base of the crust is insignificant. Faulting style is consistent with stress buildup resulted from the interseismic loading. The first-order patterns of stress and strain-rate axes at the crust are generally correlated with the plate motion. To further elucidate characteristics of regional structures, we examine areas with sufficient GPS data and earthquake focal mechanisms to detect more subtle variations. These variations may result from regional tectonics, the lithosphere flexural stress due to sediment loading in the continental margin, localized lateral strength contrast associated with material properties, and lateral strength contrast in response to the fault zone (Zoback, 1992).

In western Taiwan, the trends of maximum contraction axes and principal compressive axes (Fig. 6) are consistent with a fan-shaped pattern that has been demonstrated from various data sets (Suppe

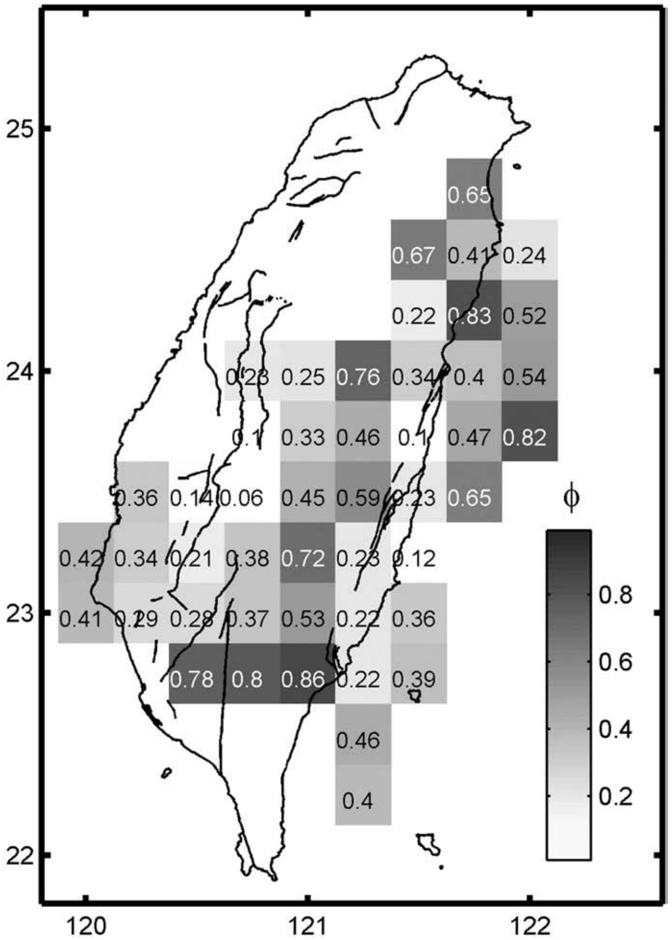

Fig. 7. Grey color and texts denote the ratio of principal stress difference $\phi = \frac{\sigma_2 - \sigma_3}{\sigma_1 - \sigma_3}$ from the stress tensor inversion. If $\sigma_1 = \sigma_2$, namely $\phi = 1$, corresponds to a stress regime transitional to normal faulting; while if $\sigma_2 = \sigma_3$, namely $\phi = 0$, corresponds to a stress regime transitional to thrust faulting.

et al., 1985; Angelier et al., 1986; Yeh et al., 1991; Bos et al., 2003; Chang et al., 2003). The fan-shaped distribution of maximum contraction and compressive axes are primary influenced by the indenter, the Peikang High (Meng, 1971), in the Chinese continental margin (Hu et al., 1996). To examine this hypothesis, we compare the shape of the West Taiwan foreland basin (Fig. 4d) with orientations of maximum contraction and compressive axes. The Peikang High is located on the western fringe of the foreland basin (Fig. 4d). Seismic and well data suggest that the West Taiwan foreland basin developed by orogenic loading and flexure of a rift-type continental margin (Lin and Watts, 2002). We find that the shape of the foreland is only partially correlated with the trend of maximum contraction or compressive axes (Figs. 4c,d, and 6); therefore, other explanations different from the shape of the Chinese continental margin need to be investigated. Lin and Watts (2002) interpreted that the low and active seismicity on the northern and southern Taiwan foreland basin reflect low and high bending stress due to the curvature of the foreland basin, respectively. The base (~8 km) of the foreland basin is the greatest near Tainan and Kaohsiung areas. The flexural stress due to sediment loading could induce margin-normal extensional stress on the loaded continental shelf and margin-normal compression in the adjacent regions (Stein et al., 1989). Limited by the complex shape of the Chinese continental margin near Tainan and Kaohsiung (Fig. 4d), we cannot find a simple correlation between the shape of the Chinese continental margin and orientations of stress or strain-rate axes. A numerical model is needed to further clarify the impact of the sediment loading in the future.

In addition, the trends of σ_1 and contraction axes in the Coastal Plain and the Western Foothills between Chiayi and Kaohsiung, are perceptible different by about 20°–40° from those in the southern Central Range (Fig. 6). Regions near SW Taiwan may be experiencing lateral extrusion (Lu and Malavieille, 1994; Lacombe et al., 2001; Bos et al., 2003; Gourley, 2006; Gourley et al., 2007; Hu et al., 2007). To what extent this lateral-escape tectonic model explains the rotations of σ_1 and contraction axes remains unclear. The strength of crustal material may be very different in SW Taiwan and the southern Central Range, and could provide another source for the rotation of compressive or contraction axes. Earlier studies show that the upper crust of SW Taiwan is composed of the sedimentary wedge (Lacombe et al., 2001) and the P wave velocity is low comparing to that in adjacent regions (Kim et al., 2005; Wu et al., 2007). In contrast to Pre-Tertiary metamorphic complex in the Central Range, the sediments in SW Taiwan are too weak to produce earthquakes at shallow depths (Fig. 8). In summary, we hypothesize that the sharp variations of strain-rate and stress axes between SW Taiwan and the southern Central Range could be associated with the tectonic escape in SW Taiwan as well as the lateral strength contrast due to different geological materials.

Significant extension in northeastern Taiwan (Ilan plain) and the Central Range is inferred from GPS velocity field in this study and some previous work (Bos et al., 2003; Chang et al., 2003). The result of stress tensor inversion in the Ilan plain shows that the σ_1 axis and the σ_3 axis are vertically- and horizontally-oriented, respectively (Fig. 5), consistent with a normal-faulting stress regime. The direction of the tension is consistent with the NW–SE extension derived from GPS velocities. The extension in the Ilan plain is associated with the opening of Okinawa Trough (Sibuet et al., 1987). In terms of the extension in the Central Range, it is mainly constrained by GPS velocities due to limited seismicity in the northern portion of the Central Range. Previous studies proposed different hypothesis to explain the extension of the Central Range, including the crustal exhumation due to the increase of buoyancy forces on the light subducted continental crust (Lin, 2000), the current collision between the PSP and the basement high on the EUP (Gourley et al., 2007) as well as the lateral extrusion is SW Taiwan (Gourley, 2006). We suggest that the extension in the Central Range may be a result of exhumation associated with overthickened continental crust and the buoyancy force of the subducted continental crust (Lin, 2000). The exhumation in the Central Range may be due to gravitational collapse of the upper most crust. Results from fission track ages (Liu, 1982) inferred that the uplift of the Central Range has increased rapidly since about 3 Ma ago to an average of 9 mm/yr during the last 0.6 Ma. The crustal thickening corresponding to high topography has been inferred from seismic tomography studies (Kim et al., 2005; Wu et al., 2007). We expect that a negative density anomaly associated the root of the thickened crust would produce extensional stress and strain, as has been seen in other orogenies such as the Andes and the Himalayas (Zoback, 1992). Results from the thermokinematic model of the Taiwan mountain belt suggest that crustal thickening and exhumation are sustained by underplating beneath the eastern part of the Central Range (Simoes et al., 2007).

In eastern Taiwan, the deformation is primary taken up by left-lateral oblique thrust faulting in LVF (Yu and Kuo, 2001). We find a counterclockwise rotation of σ_1 axis from the northern to southern Longitudinal Valley, a similar pattern is found in strain-rate contraction axes (Fig. 6). The azimuthal changes of principal compressive axes might be correlated with the change of subduction polarity in northern and southern Taiwan (Figs. 1 and 8).

4.4. The crustal stress field derived from seismicity and focal mechanisms

We find that most shallow earthquakes are located near the mountain front in western Taiwan (Fig. 8). Previous study in the Himalaya shows that the high topography affects the seismicity

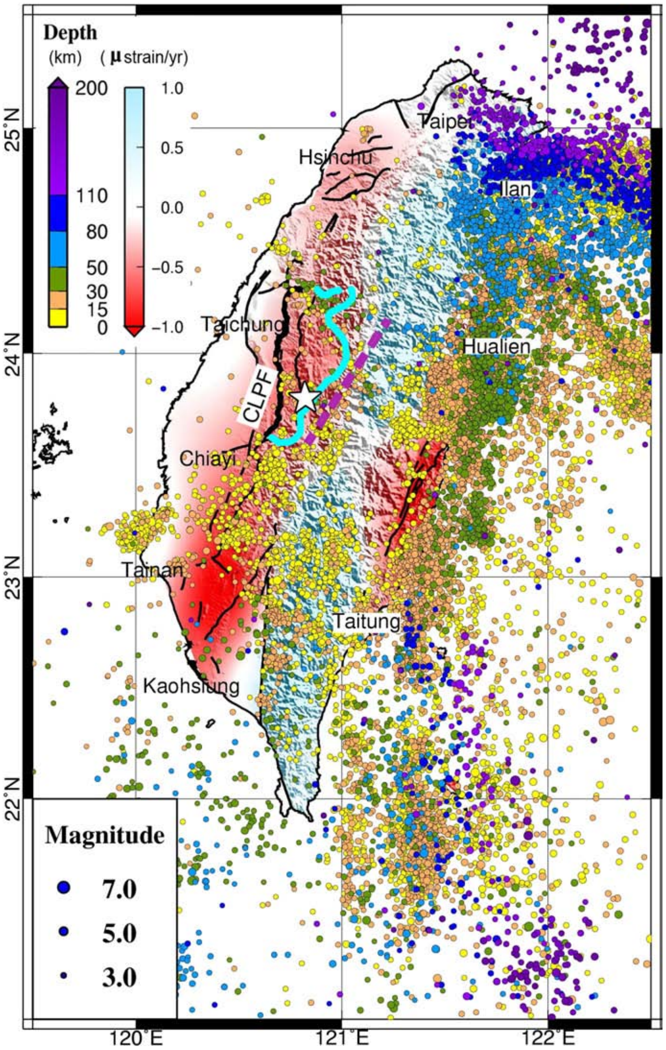

Fig. 8. The seismicity and dilatation rate in the Taiwan area. The seismicity with $M_L > 3$ between 1990 and 1999.7 is located by the Central Weather Bureau (CWB) seismic network in Taiwan. Color circle indicates earthquake focal depth and its size is proportional to the magnitude. The red and blue colors show the dilatation field in Fig. 4c. The area between the CLPF and the light blue line indicates the region where the Chi-Chi coseismic slip is larger than 1 m. The purple dash line shows the western end of interseismic slip on the décollement from Hsu et al. (2003).

distribution (Bollinger et al., 2004). To evaluate the impact of high topography on the seismicity pattern in Taiwan, we examine seismicity and earthquake focal mechanisms with $M_L > 4$ and depth < 30 km (Wu et al., 2008) before and after the Chi-Chi earthquake (Fig. 9). Seismicity near the northeastern CLPF and the northern portion of eastern Central Range (A in Fig. 9b) is quiescent before the Chi-Chi earthquake; while the seismicity becomes active after the Chi-Chi earthquake (Fig. 9). Many normal-faulting earthquakes occur in the Central Range after the Chi-Chi mainshock (A in Fig. 9b). This feature could be an indication of the rotation of maximum principal stress axis from horizontally- to vertically-oriented in response to the high topography. The inferred maximum principal stress (σ_1) in these regions is close to vertical and the minimum principal stress (σ_3) is parallel to the direction of plate motion as indicated in a simple Mohr circle diagram (A in Fig. 10a). Before the Chi-Chi earthquake, the increase of NW–SE directed convergence between the EUP and the PHP (equivalent to the increase of horizontal principal stress σ_3) prohibit fault failures. After the Chi-Chi earthquake, the decrease of NW–SE compression induced normal faulting (A in Fig. 9a). The aseismic zone near the middle part of the Central Range (B in Fig. 9b) implies that σ_1 is close to vertical, and σ_2 is parallel to the direction of plate convergence (Fig. 10). The intermediate stress, σ_2, increases and decreases before and after the mainshock, respectively. However, the magnitude of σ_2 has no influence on fault failures (B in Fig. 10a). The seismic activity is always low beneath the middle part of the Central Range (Fig. 9). The strike–slip and normal faulting near the southern Central Range (C in Fig. 9b) suggest that the magnitude of σ_1 is close to σ_2 (Fig. 10b). There are more strike–slip events than normal events in southern Central Range before the Chi-Chi earthquake; while after the Chi-Chi earthquake, we find the opposite (more normal events than strike–slip events) (Fig. 9). This implies that the σ_1 become more aligned with the vertical direction after the Chi-Chi earthquake. Indeed, we find that the ratio of principal stress difference, ϕ, is close to 1 in southern Central Range before the Chi-Chi mainshock (Fig. 7). This represents a transitional stress regime of strike–slip faulting to normal faulting that required only minor stress fluctuations in stress magnitude to change from one stress regime to the other. Regions with elevations lower than ~1500 m, for instance, the Western Foothills and the Longitudinal Valley (D, E in Fig. 9b), show little effect in topography that σ_1 axes are the maximum horizontal compressive stress. The focal mechanisms include both thrust-faulting and strike–slip faulting. The faulting style does not vary a lot before and after the Chi-Chi mainshock. The inferred directions of principal stress axes in Taiwan are summarized in Fig. 10b.

The state of the inferred crustal stress field could be used in seismic cycle modeling as a priori constrains from independent studies. In addition, we provide constraints for the orientation of the regional stress which is a key parameter in studies of Coulomb stress change (Toda et al., 1998). Our results also can apply to the estimates of stress magnitude in the crust by examining how regional stress field react to the stress perturbations from large earthquakes.

5. Interseismic strain rates near the rupture area of the 1999 Chi-Chi earthquake

One major goal of using the strain rate field in our study is to identify regions with potential seismic hazards. We are particular interested in seeking for variations of strain-rate and seismicity before the 1999 M_w 7.6 Chi-Chi earthquake. This earthquake nucleated at 8–10 km depth and generated a 100 km-long surface rupture. Yu et al. (2001) analyze preseismic GPS data and conclude that there are no abnormal signals in GPS position time series before the occurrence of the Chi-Chi earthquake. Therefore, we focus on investigating the spatial variation of the secular strain-rate and seismicity using GPS observations and earthquake data before the Chi-Chi mainshock.

The region near the Chi-Chi coseismic rupture is characterized with a moderate shortening rate of 25 mm/yr in a 40-km-wide zone from eastern boundary of the Western Foothill to the Coastal Plain (Fig. 4c). The most distinct feature in this region is that areas with high seismicity (mostly $M_L < 4$) surround the Taichung basin in the interseismic period (Fig. 8). The location of this seismic zone indicates the boundary of the contraction area to the west and the extension area to the east in central Taiwan (Fig. 8). This seismic zone is also consistent with the location of western limit of décollement (Fig. 8) that slips at a rate of about 30 mm/yr over the interseismic period (Dominguez et al., 2003; Hsu et al., 2003). Because of high stress concentration on the tip of décollement, the level of small magnitude seismic activity is high. Previous kinematic modeling using interseismic GPS velocity field suggests that the western end of the décollement is the locked area where major earthquakes might occur (Dominguez et al., 2003; Hsu et al., 2003), and their results are surprisingly consistent with the rupture area of the Chi-Chi earthquake (Fig. 8). Our study infers a high contraction rate of about 0.6 µstrain/yr in central Taiwan corresponding to the Chi-Chi rupture area as well.

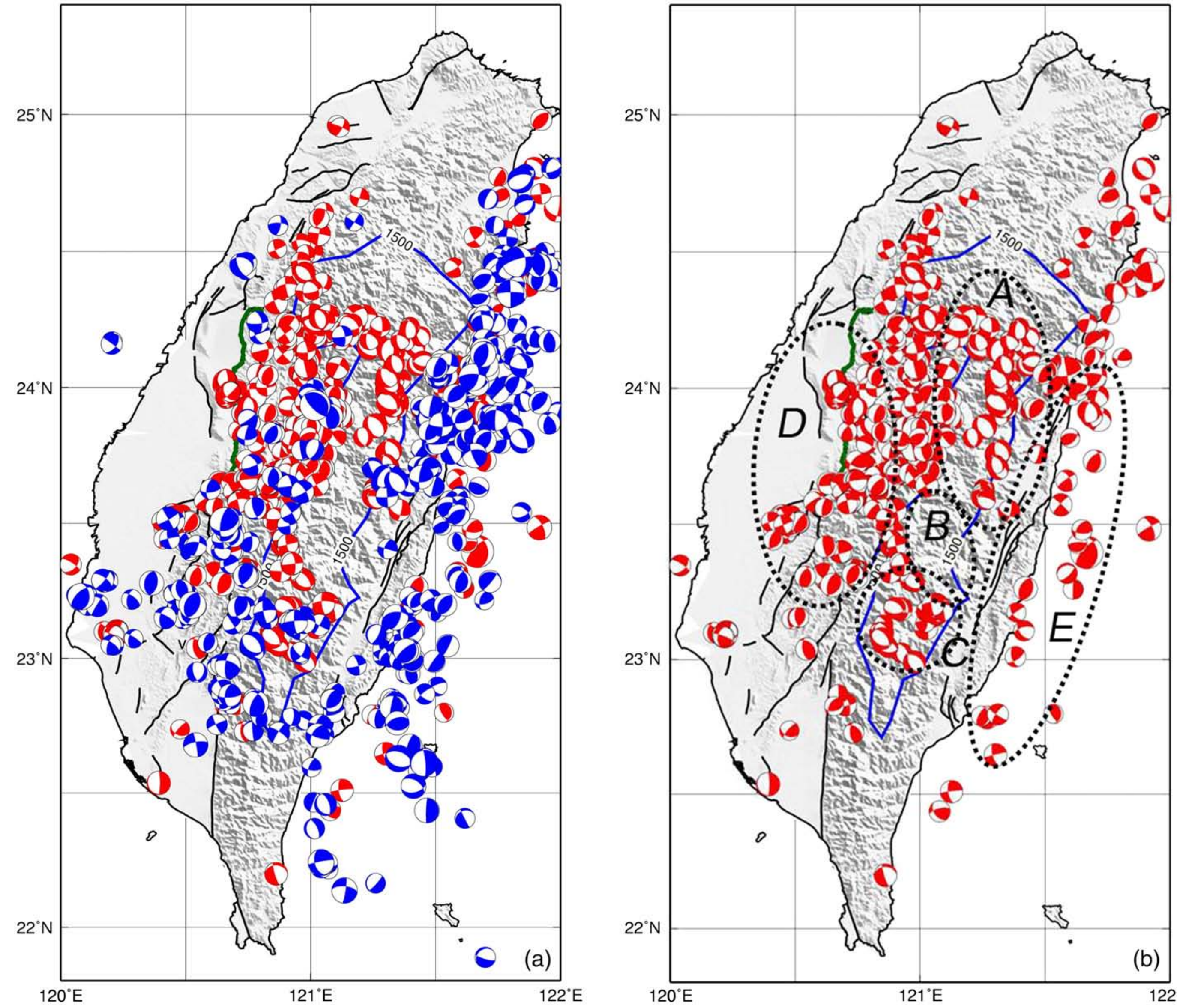

Fig. 9. Earthquake focal mechanisms with $M_L>4$ and depth <30 km from Wu et al. (2008) (a) Focal mechanisms before and after 1999.7 (the Chi-Chi earthquake) are shown as blue and red, respectively; The green and blue lines denote the CLPF and the elevation of 1500 m, respectively; (b) Focal mechanisms between 1999.7 and 2001.7 (after the Chi-Chi earthquake).

It is worth noting that the strain rate in the rupture area of Chi-Chi earthquake is not the largest, in particular, rates are higher in SW Taiwan and the Longitudinal Valley. The interseismic strain rate may be greater than the average strain rate of the seismic cycle after the earthquake; while it becomes smaller than the average before the next future earthquake (Segall, 2002). Obviously, areas with small strain rate in the interseismic period still have potential to generate large earthquakes, either they are in a late stage of the seismic cycle or they need longer strain accumulation period.

We find most shallow earthquakes locate near the mountain front in western Taiwan; while the shallow seismicity primary distribute to the east of the Coastal Range in eastern Taiwan (Fig. 8). According to the historic earthquakes in past century and the characteristics of seismicity distribution in central Taiwan, small earthquakes tend to surround the locked fault zone in the interseismic period. The future earthquake probabilities are high in the western Taiwan and the Longitudinal Valley. To have a better estimate of possible earthquake rupture sources in these regions, we need to carefully investigate all available geodetic, seismological, as well as geological data.

6. Conclusion

We use the interseismic GPS velocity field between 1993 and 1999 to estimate the strain-rate field. Our new approach of strain-rate calculation takes account of the contribution of variable station density from the distribution of Voronoi cells and avoids dominating results by dense pockets of observations. The strain-rate field shows that the Longitudinal Valley and SW Taiwan have high NW–SE-directed contraction in contrast to high NW–SE to NEE–SWW-directed extensions in NE Taiwan and southern Central Range, respectively. The first-order pattern of the strain-rate field is consistent with previous studies. In addition, we conduct the stress tensor inversion using earthquake focal mechanisms to obtain the crustal stress field. The consistency of orientations in principal strain-rate and stress axes suggests that a large scale variation of stress orientations from the surface to the base of the crust is insignificant. The stress and strain-rate axes in western Taiwan show a fan-shaped pattern. However, we find that the shape of the Chinese continental margin alone cannot fully explain

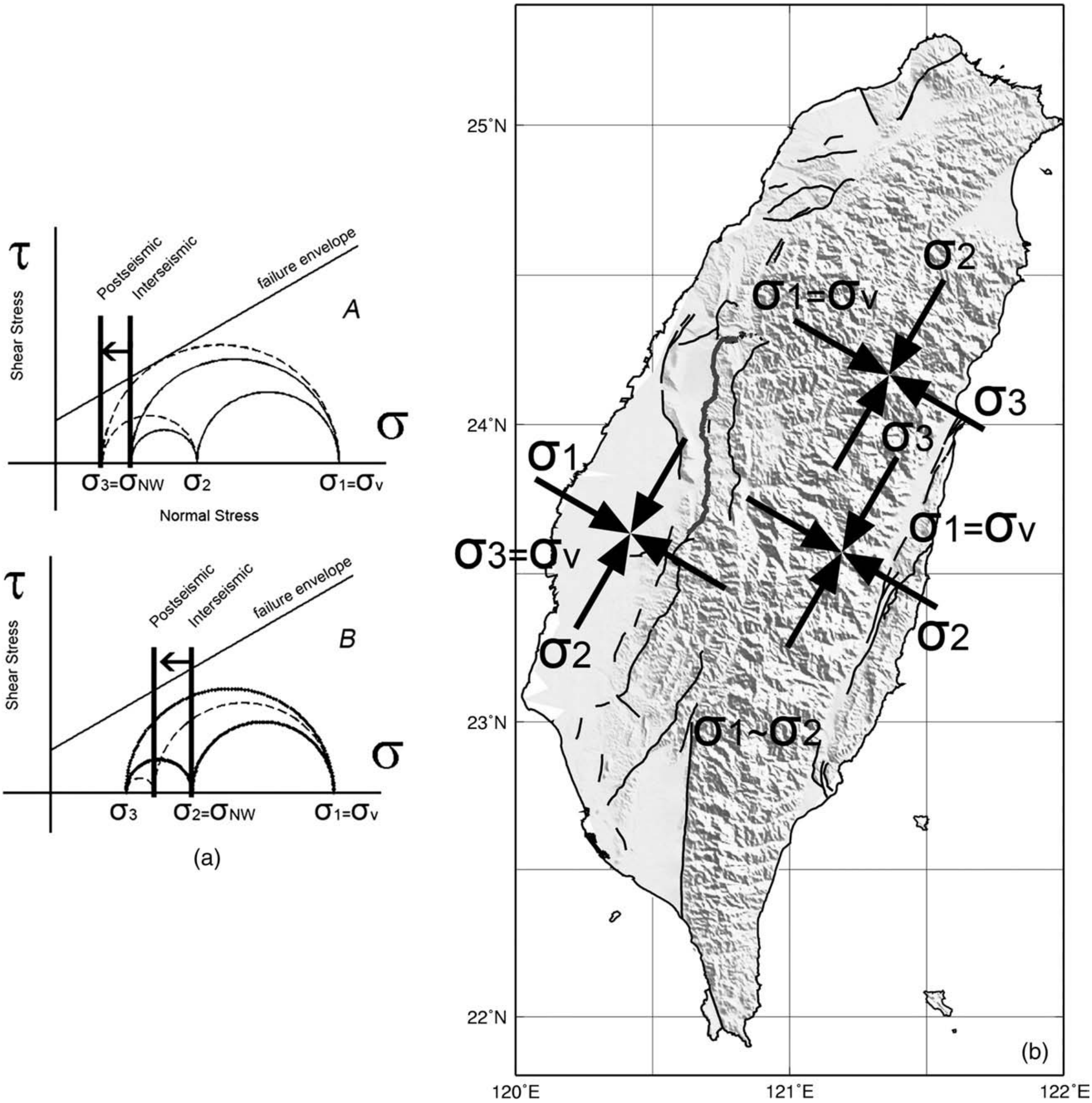

Fig. 10. The orientations of principal stress axes (a) The Mohr circle represents the stress of the crust in area A and B denoted in Fig. 9b. The straight line indicates the strength of the crust; (b) Inferred stress axes from seismicity distribution and focal mechanisms.

the distribution of maximum contractive and compressive axes in Taiwan. Extension in the Central Range reflects the consequence of exhumation and crustal thickening. The seismicity and focal mechanisms before and after the Chi-Chi earthquake imply that the high topography in the Central Rage has changed the maximum principal stress axis to be vertically orientated. Analyses of geodetic and seismological data before the 1999 Chi-Chi earthquake show the consistency between the inferred locked zone and the Chi-Chi coseismic rupture area. Integrating studies using all available data is important to shed new light on earthquake rupture sources.

Acknowledgments

We are grateful to many colleagues at the Institute of Earth Sciences, Academia Sinica who have participated in collecting GPS data. The generous provision of continuous GPS data by Ministry of the Interior, National Cheng-Kung University, National Chiao-Tung University and IGS community is greatly appreciated. We thank the editor, Dr. D. Brown, Dr. J. Malavieille and an anonymous reviewer for their constructive comments, Y. M. Wu kindly provides earthquake focal mechanisms, J.-P. Avouac and W. T. Liang provide valuable suggestions. Several figures were created using GMT written by Wessel and Smith. This study is supported by the Institute of Earth Sciences, Academia Sinica, the National Science Council of the Republic of China grant NSC 95-2119-M-001-064-MY3 and NSC 95-2745-M-001-005, the National Science Foundation grant EAR-0537625 to Caltech, and the Gordon and Betty Moore Foundation. This is a contribution of the Institute of Earth Sciences, Academia Sinica, IESAS1287, Caltech Seismological Laboratory contribution number 10004, and Caltech Tectonics Observatory number 84.

References

Angelier, J., Barrier, E., Chu, H.T., 1986. Plate collision and paleostress trajectories in a fold thrust belt — the foothills of Taiwan. Tectonophysics 125, 161–178.

Barrier, E., Angelier, J., 1986. Active collision in eastern Taiwan — the Coastal Range. Tectonophysics 125, 39–72.

Biq, C.C., 1972. Dual trench structure in the Taiwan–Luzon region. Proc. Geol. Soc. China 15, 65–75.

Bollinger, L., Avouac, J.P., Cattin, R., Pandey, M.R., 2004. Stress buildup in the Himalaya. J. Geophys. Res. 109. doi:10.1029/2003JB002911.

Bos, A.G., Spakman, W., Nyst, M.C.J., 2003. Surface deformation and tectonic setting of Taiwan inferred from a GPS velocity field. J. Geophys. Res. 108. doi:10.1029/2002JB002336.

Chang, C.P., Chang, T.Y., Angelier, J., Kao, H., Lee, J.C., Yu, S.B., 2003. Strain and stress field in Taiwan oblique convergent system: constraints from GPS observation and tectonic data. Earth Planet. Sci. Lett. 214, 115–127.

Crespi, J.M., Chan, Y.C., Swaim, M.S., 1996. Synorogenic extension and exhumation of the Taiwan hinterland. Geology 24, 247–250.

Dominguez, S., Avouac, J.P., Michel, R., 2003. Horizontal coseismic deformation of the 1999 Chi-Chi earthquake measured from SPOT satellite images: implications for the seismic cycle along the western foothills of central Taiwan. J. Geophys. Res. 108. doi:10.1029/2001JB000951.

Gourley, J. R., 2006. Syn-tectonic extension and lateral extrusion in Taiwan: the tectonic response to a basement high promontory, University of Connecticut, Ph.D. dissertation, pp.129.

Gourley, J.R., Byrne, T., Chan, Y.C., Wu, F., Rau, R.J., 2007. Fault geometries illuminated from seismicity in central Taiwan: implications for crustal scale structural boundaries in the northern Central Range. Tectonophysics 445, 168–185.

Ho, C.S., 1986. A synthesis of the geologic evolution of Taiwan. Tectonophysics 125, 1–16.

Hsu, T.L., 1976. Neotectonics of the Longitudinal Valley, eastern Taiwan. Bull. Geol. Surv. Taiwan 25, 53–62.

Hsu, Y.J., Simons, M., Yu, S.B., Kuo, L.C., Chen, H.Y., 2003. A two-dimensional dislocation model for interseismic deformation of the Taiwan mountain belt. Earth Planet. Sci. Lett. 211, 287–294.

Hu, J.C., Angelier, J., Lee, J.C., Chu, T.H., Byrne, D., 1996. Kinematics of convergence, deformation and stress distribution in the Taiwan collision area: 2-D finite-element numerical modelling. Tectonophysics 255, 243–268.

Hu, J.C., Hou, C.S., Shen, L.C., Chan, Y.C., Chen, R.F., Huang, C., Rau, R.J., Chen, K.H.H., Lin, C.W., Huang, M.H., Nien, P.F., 2007. Fault activity and lateral extrusion inferred from velocity field revealed by GPS measurements in the Pingtung area of southwestern Taiwan. J Asian Earth Sci 31, 287–302.

Huang, C.Y., Wu, W.Y., Chang, C.P., Tsao, S., Yuan, P.B., Lin, C.W., Xia, K.Y., 1997. Tectonic evolution of accretionary prism in the arc-continent collision terrane of Taiwan. Tectonophysics 281, 31–51.

Hugentobler, U., Schaer, S., Fridez, P., 2001. Bernese GPS Software v. 4.2, Astronomical Institute. University of Berne, Switzerland. 515pp.

Kao, H., Jian, P.R., 2001. Seismogenic patterns in the Taiwan region: insights from source parameter inversion of BATS data. Tectonophysics 333, 179–198.

Kim, K.H., Chiu, J.M., Pujol, J., Chen, K.C., Huang, B.S., Yeh, Y.H., Shen, P., 2005. Three-dimensional V-P and V-S structural models associated with the active subduction and collision tectonics in the Taiwan region. Geophys. J. Int. 162, 204–220.

Lacombe, O., Mouthereau, F., Angelier, J., Deffontaines, B., 2001. Structural, geodetic and seismological evidence for tectonic escape in SW Taiwan. Tectonophysics 333, 323–345.

Lin, C.H., 2000. Thermal modeling of continental subduction and exhumation constrained by heat flow and seismicity in Taiwan. Tectonophysics 324, 189–201.

Lin, A.T., Watts, A.B., 2002. Origin of the West Taiwan basin by orogenic loading and flexure of a rifted continental margin. J. Geophys. Res. 107.

Liu, T.K., 1982. Tectonic implication of fission track ages from the Central Range. Taiwan, Proc. Geol. Soc. China, 25, 22–37.

Lu, C.Y., Malavieille, J., 1994. Oblique convergence, indentation and rotation tectonics in the Taiwan mountain belt — insights from experimental modeling. Earth Planet. Sci. Lett. 121, 477–494.

Matthews, M.V., Segall, P., 1993. Estimation of depth-dependent fault slip from measured surface deformation with application to the 1906 San-Francisco earthquake. J. Geophys. Res. 98, 12153–12163.

Meng, G.Y., 1971. A conception of the evolution of the island of Taiwan and its bearing on the development of the western Neogene sedimentary basin. Petrol. Geol. Taiwan 9, 241–258.

Michael, A.J., 1984. Determination of stress from slip data — faults and folds. J. Geophys. Res. 89, 1517–1526.

Michael, A.J., 1987. Use of focal mechanisms to determine stress — a control study. J. Geophys. Res. 92, 357–368.

Segall, P., 2002. Integrating geologic and geodetic estimates of slip rate on the San Andreas fault system. Int. Geology Rev. 44, 62–82.

Seno, T., Stein, S., Gripp, A.E., 1993. A model for the Motion of the Philippine Sea Plate consistent with Nuvel-1 and geological Data. J. Geophys. Res. 98, 17941–17948.

Shen, Z.K., Jackson, D.D., Ge, B.X., 1996. Crustal deformation across and beyond the Los Angeles basin from geodetic measurements. J. Geophys. Res. 101, 27957–27980.

Sibuet, J.C., Letouzey, J., Barbier, F., Charvet, J., Foucher, J.P., Hilde, T.W.C., Kimura, M., Chiao, L.Y., Marsset, B., Muller, C., Stephan, J.F., 1987. Back arc extension in the Okinawa trough. J. Geophys. Res. 92, 14041–14063.

Simoes, M., Avouac, J.P., Beyssac, O., Goffe, B., Farley, K.A., Chen, Y.G., 2007. Mountain building in Taiwan: a thermokinematic model. J. Geophys. Res. 112. doi:10.1029/2006JB004824.

Stein, S., Cloetingh, S., Sleep, N.H., Wortel, R., 1989. Passive margin earthquakes, stresses and rheology. Earthquakes at North-Atlantic passive margins: neotectonics and postglacial respond, NATO ASI Ser. C. Kluwer Academic, Boston, Mass., pp. 231–259.

Suppe, J., 1984. Kinematics of arc-continent collision, flipping of subduction, and back-arc spreading near Taiwan. Mem. Geol. Soc. China 21–33.

Suppe, J., Hu, C.T., Chen, Y.J., 1985. Preset-day stress directions in western Taiwan inferred from borehole elongation. Petrol. Geol. Taiwan 21, 1–12.

Teng, L.S., 1996. Extensional collapse of the northern Taiwan mountain belt. Geology 24, 949–952.

Toda, S., Stein, R.S., Reasenberg, P.A., Dieterich, J.H., Yoshida, A., 1998. Stress transferred by the 1995 M-w = 6.9 Kobe, Japan, shock: effect on aftershocks and future earthquake probabilities. J. Geophys. Res. 103, 24543–24565.

Ward, S., 1998. On the consistency of earthquake moment rates, geological fault data, and space geodetic strain: the United States. Geophys. J. Int. 134, 172–186.

Wu, F.T., 1978. Recent tectonics in Taiwan. J. Phys. Earth 26, 265–299.

Wu, Y.M., Chang, C.H., Zhao, L., Shyu, J.B.H., Chen, Y.G., Sieh, K., Avouac, J.P., 2007. Seismic tomography of Taiwan: improved constraints from a dense network of strong motion stations. J. Geophys. Res. 112. doi:10.1029/2007JB004983.

Wu, Y.M., Zhao, L., Chang, C.H., Hsu, Y.J., 2008. Focal-mechanism determination in Taiwan by genetic algorithm. Bull. Seismol. Soc. Am. 98, 651–661.

Yeh, Y.H., Barrier, E., Lin, C.H., Angelier, J., 1991. Stress tensor analysis in the Taiwan area from focal mechanisms of earthquakes. Tectonophysics 200, 267–280.

Yu, S.B., Chen, H.Y., 1994. Global Positioning System measurements of crustal deformation in the Taiwan arc-continent collision zone. TAO 5, 477–498.

Yu, S.B., Kuo, L.C., 2001. Present-day crustal motion along the Longitudinal Valley Fault, eastern Taiwan. Tectonophysics 333, 199–217.

Yu, S.B., Chen, H.Y., Kuo, L.C., 1997. Velocity field of GPS stations in the Taiwan area. Tectonophysics 274, 41–59.

Yu, S.-B., Kuo, L.-C., Hsu, Y.-J., Su, H.-H., Liu, C.C., Hou, C.-S., Lee, J.-F., Lai, T.-C., Liu, C.C., Liu, C.-L., Tseng, T.-F., Tsai, C.-S., Shin, T.-C., 2001. Preseismic deformation and coseismic displacements associated with the 1999 Chi-Chi, Taiwan, earthquake. Bull. Seismol. Soc. Am. 91, 995–1012.

Zoback, M.L., 1992. First- and second-order patterns of stress in the lithosphere: the world stress map project. J. Geophys. Res. 97, 11703–11728.